A preliminary study for an intraoperative 3D bioprinting treatment of severe burn injuries.

Marion Albouy
  Labskin Creations

Adeline Desanlis
  Hospices Civils de Lyon

Sophie Brosset
  Hospices Civils de Lyon

Celine Auxenfans
  Hospices Civils de Lyon

Edwin-Joffrey Courtial
  3d.FAB-UMR5246

Kyle Eli
  Advanced Solutions Life Sciences

Scott Cambron
  Advanced Solutions Life Sciences

Justin Palmer
  Advanced Solutions Life Sciences

Luciano Vidal
  Rapid Manufacturing Platform, Centrale Nantes

Amélie Thépot
  Labskin Creations

Morgan Dos Santos
  Labskin Creations

Marquette Christophe (✉ christophe.marquette@univ-lyon1.fr)
  3d.FAB-UMR5246   https://orcid.org/0000-0003-3019-0696

Abstract

Background: Intraoperative three-dimensional (3D) fabrication of living tissues could be the next biomedical revolution in patient treatment.

Approach: We developed a surgery-ready robotic 3D bioprinter and demonstrated that a bioprinting procedure using medical grade hydrogel could be performed using a 6-axis robotic arm *in vivo* for treating burn injuries.

Results: We conducted a pilot swine animal study on a deep third-degree severe burn model. We observed that the use of cell-laden bioink as treatment substantially affects skin regeneration, producing *in situ* fibroblast growth factor (FGF) and vascular endothelial growth factor (VEGF), necessary for tissue regeneration and re-epidermalization of the wound.

Innovation and Conclusion: We described an animal study of intraoperative 3D bioprinting living tissue. This emerging technology brings the first proof of *in vivo* skin printing feasibility using a surgery-ready robotic arm-based bioprinter. Our positive outcome in skin regeneration, joined with this procedure's feasibility, allow us to envision the possibility of using this innovative approach in a human clinical trial in the near future.

Introduction

Skin is the largest organ in the human body, which protects all other tissues from the environmental challenges, infections, and mechanical stresses. Severe burn injuries of skin are difficult to manage due to multiple problems ranging from pain to infection and scars. When a burn affects the skin's extended surface, the vital emergency is to restore the skin barrier to prevent sepsis and significant fluid loss [1]. In this case, early surgical excision and autologous skin grafting remain the standard of care [2, 3]. However, the limit of this technique is the low availability of healthy skin [4]. Allografts, taken from a living or deceased human donor, can be used as a temporary wound coverage as they promote re-epithelialization and prepare the wound bed for autograft. Nevertheless, allograft rejection is likely to occur within two weeks [5] if not replaced by an autograft. Conversely, cultured autologous epidermis assures a permanent wound coverage, but requires specialized infrastructure and allows epidermis reconstruction but without dermis.

Bringing an innovative approach to the field, we developed and tested a concept of *in vivo* skin bioprinting. In this concept, a 6-axis robotic arm bioprinter is deployed into the surgery theatre and used to print directly on skin wounds. The present report describes the conceptual and experimental steps which led to the validation of the concept in a preliminary, pre-clinical pilot study. In this conceptual approach, a single cellularized bioink is printed over the entire wound surface and facilitates regeneration of the damaged dermis and epidermis layers. The bioink, previously published by our group [6, 7], was shown to trigger fibroblasts and endothelial cells proliferation. This property was used herein to accelerate deep burn wound *in situ* regeneration. The addition of dermal fibroblasts to the bioink was expected to bring a

combined effect through the *in situ* generation of growth factors including VEGF, FGF and platelet-derived growth factor (PDGF) [8-12], involved in the different stage of the wound healing (migration, proliferation and extracellular matrix synthesis).

Conceptual Approach

Bioprinting on a living subject in order to reconstruct non-standardized wounds or defects requires a high degree of movement freedom of the bioprinting tool [13]. Unlike commercially available bioprinters with three-axis coordinates, robotic arms (such as surgical robots) can be the ideal solution to print on irregular-shaped surfaces efficiently. Here, the BioAssemblyBot®, with its six-axis robotic arm, from Advanced Solutions Inc., is currently the only commercially available bioprinter with a high degree of necessary freedom for such *in situ* applications.

For the present pilot *in vivo* experiment, the BioAssemblyBot® was customized to accommodate printing onto the skin surface of a subject outside the initial enclosure to operate directly on top of an operating table (**Figure 1-A**). A novel safety enclosure was designed, which enabled the secure operation of the robotic arm while reaching the much larger surgical arena created at the back side of the machine (**Figure 1-B**). Once the hardware modification concept validated, a special arm displacement routine was implemented to bioprint safely outside of the initial enclosure.

The final surgery-ready BioAssemblyBot® was then able to reach an area of 0.5 m² outside the initial enclosure while maintaining 20 micron precision. This area was large enough to facilitate *in vivo* bioprinting on a standard animal surgical core facility.

Experimental Strategy

After preparation of the subject, bioprinting on the target surface of the anesthetized subject was performed with the following steps: the printing-surface contour data was acquired, a digital model of the printing-surface was created, the skin patch to be printed was designed in the context of the subject-specific contours, and the skin patch was bioprinted.

An example of a typical bioprinting process may use a dispensing tool with a fixed, coordinate-system aligned orientation and target a precisely fabricated and calibrated target subject surface (e.g. an adjustable plate) that can then be modelled in software with an equation of a plane that shares an origin and orientation with the printer coordinate system. When working with more capable tooling, which allows for additional degrees of freedom in dispensing tool placement (when compared to a traditional 3-axis printer) as well as targeting the printing surface of a living subject, a relative increasing in complexity of the target surface topology may suggest the use of a different modeling approach to facilitate an adequate level of accuracy in the alignment-between the surface normal and tool orientation as well as the distance from the tooltip to the target surface during path planning and execution. For this

experiment, structured elevation sampling and interpolation were used to measure and model the target surface topology.

Acquiring the surface elevation ("scanning") involved sampling the elevation of the surface with a displacement sensor placed at regular intervals along a planar structured grid aligned with the printer coordinate system X-Y plane. The machine user provides a region of interest, tool offset from the printer coordinate system X-Y plane, and grid spacing. The user may then execute a printer function that moves the displacement sensor around the perimeter of the given region of interest, allowing the user to review and correct errors before executing the scan. When scanning, the robotic arm moves the displacement sensor to a grid intersection and then waits to acquire a stable elevation sample before moving on to the next intersection. Each grid intersection is visited once, with the printer's resulting data set until the user requests a download.

After downloading the surface data (**Figure 1-D**) to the computer-aided design TSIM (Tissue structure information modelling) software used for this experiment, it is presented to the user in the form of a shaded triangulated mesh model. When working with a living subject, requirements may preclude mapping the scanned surface topology in the design software coordinate system to the real-world surface in the printer coordinate system. To do so, we were executing short printing operations to measure the difference between the coordinate systems. For this experiment, the specified high-resolution repeatability of the robotic manipulator carrying the displacement sensor tool was leveraged to create the mapping separately and before the living subject was interfaced with the printer. This mapping produced from a different subject provided an adequate accuracy level when executing the final printing operation.

After creating the mapping between the coordinate design system and the printer coordinate system, completing the interface between the printer and the living subject, and finally scanning and downloading the surface topology, the print design process can begin. During the design process, the surface model was modified to remove areas of the surface mesh with high levels of noise and bound the surface to the region of interest used for creating the printed design. The surface model was exported from TSIM using the standard "STL" format and then cropped using a triangulated mesh editing software system before being re-imported into TSIM (**Figure 1-D**). After importing the modified surface into TSIM, coordinate system mapping was used to adjust the placement. It was accurately positioned relative to the real-world surface in the printer coordinate system.

For this experiment, the designed skin patch consisted of a series of extruded adjacent tubes to create a continuous patch filling the wound's volume on the subject (**Figure 1-D**). We used a tube patterning feature of the TSIM design software with the following parameters: tube diameter 400 μm, tube spacing 800 μm. This function also samples normal surface data from the model, which is later used by the printer to adjust the orientation of the printing tool so that it is closer to the real-world printing surface when following the printing tool path during a printing operation.

After completing the design that will be printed, TSIM was used to upload the printer's design data. Printing parameters such as printing pressure and target temperature of the dispensing tool heater were

adjusted via the human machine interface at the print time—to accommodate environmental conditions. Standard operational parameters were a pneumatic extrusion tool loaded with a 10CC cartridge (Nordson EFD, Chateou, France), equipped with a 400 µm diameter (6.3 mm long) nozzle (Nordson EFD) and an applied extrusion pressure of 10 PSI.

Figure 2-A depicts the bioink printability diagram, in which measured static yield stress (previously published method[15]) and calculated maximum shear stress (FlowTips® Program, 3d.FAB, France) were plotted as a function of temperature. In this diagram, three zones can be identified, a first one above a 5000 Pa threshold where shear stress significantly impacts cell viability [17], a second one below a 300 Pa threshold where static yield stress is not sufficient to enable 3D bioprinting fidelity [18], and a third one between these two values where 3D bioprinting of living cells is efficient. As can be seen, in the present operational conditions (400 µm diameter, 6.3 mm long nozzle, 10 PSI), both curves were in the bioprintability zone for temperature in the 21-28°C interval. It is then expected that during the pilot *in vivo* study, regulating the printing tool temperature around 28°C shall enable the efficient bioprinting of the cell-laden bioink (fibroblasts concentration: 1×10^6 cells.mL^{-1}).

Pilot Study Experimental Results

Six circular burns of 4.5 cm in diameter (i.e. an area of 15.9 cm² / burn) were carried out on the back of the pig, 2 cm from the spine, and spaced 5 cm from each other to avoid interference between the burns. Seven days after burning, removal of phlyctena was performed on all wounds were excised. Out of the 6 wounds, 2 were kept as self-healing controls without bioink (standard severe burn treatment using Silver sulfadiazine (1%)), 2 were bioprinted with bioink alone and 2 were bioprinted with fibroblast-laden bioink (250 000 cells/mL).

In the present experimental design, control wounds did not experience the presence of the bioprinting head above the wounds. Nevertheless, the bioprinting technique used (extrusion) does not generate any contact between the bioprinting head and the surface since the head is accurately flying at 800µm from the surface.

For each condition, one wound was used to perform biopsy and histology at day 11 (post-bioprinting), 21, 28, 35 and 42, while the second one was used for macroscopic evaluation.

The histological sections of the wounds were analyzed qualitatively seven days after the burn to define the affected tissues' depth. The histological results clearly showed that the degree of burn obtained was indeed a third degree, with a complete destruction of the animal's hair follicles. This profound tissue damage allowed for a full assessment of the effectiveness of the tested therapy. The **Figure 1-D** depicts the two robotic steps of the protocol, i.e. scanning the surface and bioprinting of the bioink. **Figure 2-C** presents the macroscopic observations follow up of the wounds during healing.

A clear acceleration of the wound healing was observed when treated with cellularized bioink, leading to a 10-day shift of the wound status. Between D11 and D28, the surface of the wounds and the surface of

the scars decreased faster in the presence of the cellularized bioink than in the presence of bioink alone or in the control treatment (Silver sulfadiazine (1%)). In addition, while bioink-treated and control surfaces no longer changed between D28 and D42, the scar surface in the presence of cellularized bioink continued to decrease, leading to a clear wound status difference at D42 in favour of the cellularized bioink treatment.

In fact, at D11 after the treatment, no changes were found. All wounds were raw, not epidermized and with equivalent surfaces. At D42, all wounds were healed with reduced scar tissue surfaces. Compared to D11, the percentage of scar tissue at D42 is 33% for the wound treated with the bioink containing dermal fibroblasts, 63% for the wound treated with the bioink alone and 80% for the control wound (**Figure 2-B**). Moreover, a constant drop in scar tissue area was observed from D1 to D42 for all wounds treated with cellularized bioink. Conversely, the control and bioink-treated wounds showed a slowing-down of the healing after D28.

These observations are the first evidence of the expected positive effect of our cellularized bioink for wound healing stimulation. It is also worth to mention that no distinguishing signs of inflammation, necrosis or infection were observed between the 3 wound groups. This strongly supports the assumption that the observed effects were due to the applied treatment.

This important difference observed between the fibroblast-loaded bioink and the bioink alone reveals a clear evidence of the combined effect of the secretion of growth factors [19] and the proliferative properties of the bioink. Indeed, quantification of FGF-2 and VEGF in fibroblasts culture medium (without serum), demonstrated through ELISA, showed 24 hours accumulation of at least 1.15 pg/mL and 9.96 pg/mL of FGF-2 and VEGF, respectively.

Histological and immunofluorescent analyses were performed to confirm the macroscopic observations of the accelerated healing of the wounds treated with cellularized bioink. **Figure 3-A** presents images of the Haematoxylin-Phloxin-Saffron staining of each wound during the healing period after *in vivo* bioprinting. As can be seen, whatever the treatment conditions, the burns were found to be epidermized to the centre of the wound, 21 days after bioprinting. The epidermis was organized, multi-layered and differentiated. The stratum corneum was visible but the dermal papillae had not yet been rebuilt.

Ki67 labelling, an antigen specifically found in the nucleus of proliferative cells, determined cell proliferation variations between the different treatments in the early stages of healing in the dermis and epidermis (**Figure 3-B**).

On D11 following bioprinting, Ki67 positive cells in the dermis were numerous in all treatment conditions and since no epidermis was yet formed, no positive cells were found in the epidermis. At D21, dermis Ki67 positive cell numbers strongly decreased in the control experiment while keeping a significant value in bioink and cellularized bioink conditions, indicating that epidermal cell proliferation was highly accelerated using cellularized bioink.

αSMA (αSmooth muscle actin) immunofluorescent labelling was used to identify myofibroblasts presence in the granulation tissue. The transformation of fibroblasts into myofibroblasts leads to contractile activity necessary for wound closure. However, if their presence persists, the scar becomes hypertrophic or retractile, leading to non-aesthetic results and functional failures [20, 21]. **Figure 3-C** depicts the presence of the αSMA in the different conditions. Here again, 21 days after bioprinting, a clear difference between αSMA-positive cells at D21 in the different treatments was observed, in agreement with the macroscopic observations (**Figure 3-C**). Indeed, large numbers of myofibroblasts were still found in the control treatment wound which was, as shown in **Figure 2-E**, not yet closed after 21 days. Also, in agreement with **Figure 2-D**, a clear difference was found in myofibroblast content between bioink and cellularized bioink. In the case of bioink alone, a significant number of αSMA positive cells was still found at D21, leading to a hypertrophic scar, evidenced in **Figure 2-D** by a high and stable scare tissue percentage after 28 days. Taken altogether, these findings explain why the wound closure and scar tissue percentage observed in **Figure 2** were so drastically different in the presence of bioink seeded with dermal fibroblasts.

Finally, type IV collagen immunostaining identified neovascularization in the granulation tissue and collagen accumulation in the dermal-epidermal junction (**Figure 3-D**). This antigen is mainly found in the basement membrane around the endothelium of the capillaries. During healing, blood vessels are generated by angiogenesis. This phenomenon is essential to provide the injured site with nutrients, oxygen, and inflammatory cells and allows thus cell proliferation and tissue regeneration. However, during the remodeling phase of the scar, an antiangiogenic state appeared leading to a capillary regression [22, 23]. At D11, type IV collagen was identified in all conditions but at different organisation level. In the control experiment, collagen was not organized in the microvessels basal membrane whereas in the presence of bioink, type IV collagen was located mainly in the vessel walls. Moreover, in the presence of fibroblasts in the bioink, the microvessels were found to have fully developed lumens. At D21, the dermal-epidermal junction appeared fully mature, but only in the cellularized bioink conditions. In the control experiment, no dermal-epidermal junction was visible and in the bioink experiment, only a non-organized structure was found.

Conclusion

We described an intraoperative approach for the treatment of third-degree deep burns using *in vivo* bioprinting. The use of a 6-axis robotic arm-based bioprinter was an asset, bringing the necessary degrees of freedom and high precision to the bioink deposition. Customization of laboratory bioprinter platform to fulfil surgery theatre requirements was readily performed, enabling the robotic arm and controls software to operate directly on breathing large animals. From a wound care point of view, the in situ bioprinting of a pharmaceutical grade bioink populated with dermal fibroblasts, producing *in situ* growth factors (FGF2), drastically improved healing, residual scar tissue formation and vascularization. Bioprinted cellularized bioink accelerated healing by 10 days out of 42 total days of examination.

Declarations

Disclosure: "None of the authors has a financial interest in any of the products, devices, or drugs mentioned in this manuscript."

Author's role/participation in the authorship of the manuscript.

All the authors have made substantive intellectual contribution to the development of this manuscript and meet all four criteria of authorship.

1) substantial contributions to conception and design, acquisition of data, or analysis and interpretation of data; 2) drafting the article or revising it critically for important intellectual content; 3) final approval of the version to be published; 4) Agreement to be accountable for all aspects of the work in ensuring that questions related to the accuracy or integrity of any part of the work are appropriately investigated and resolved.

References

1.   Evers, L.H., D. Bhavsar, and P. Mailander, *The biology of burn injury.* Experimental Dermatology, 2010. **19**(9): p. 777-783.

2.   Auxenfans, C., et al., *Cultured allogenic keratinocytes for extensive burns: A retrospective study over 15 years.* Burns, 2014. **40**(1): p. 82-88.

3.   Rowan, M.P., et al., *Burn wound healing and treatment: review and advancements.* Critical Care, 2015. **19**.

4.   Varkey, M., J. Ding, and E.E. Tredget, *Advances in Skin Substitutes-Potential of Tissue Engineered Skin for Facilitating Anti-Fibrotic Healing.* Journal of Functional Biomaterials, 2015. **6**(3): p. 547-563.

5.   Ehrenreich, M. and Z. Ruszczak, *Tissue-engineered temporary wound coverings. Important options for the clinician.* Acta Dermatovenerol Alp Pannonica Adriat, 2006. **15**(1): p. 5-13.

6.   Marquette, C.A., L. Pourchet, and A. Thépot, *Skin substitute production process through additive manufacturing. Application N° 15 63461 (30/12/2015).*

7.   Pourchet, L., et al., *Large 3D bioprinted tissue: Heterogeneous perfusion and vascularization.* Bioprinting, 2019. **13**: p. e00039.

8.   Zhu, W.H., et al., *The mouse aorta model: Influence of genetic background and aging on bFGF- and VEGF-induced angiogenic sprouting.* Angiogenesis, 2003. **6**(3): p. 193-199.

9.   Nehls, V., K. Denzer, and D. Drenckhahn, *Pericyte involvement in capillary sprouting during angiogenesis in situ.* Cell and Tissue Research, 1992. **270**(3): p. 469-474.

10.   Nakatsu, M.N., et al., *Angiogenic sprouting and capillary lumen formation modeled by human umbilical vein endothelial cells (HUVEC) in fibrin gels: The role of fibroblasts and Angiopoietin-1.* Microvascular Research, 2003. **66**(2): p. 102-112.

11.   Velazquez, O.C., et al., *Fibroblast-dependent differentiation of human microvascular endothelial cells into capillary-like 3-dimensional networks.* The FASEB journal : official publication of the Federation of American Societies for Experimental Biology, 2002. **16**(10): p. 1316-1318.

12.   Chen, X., et al., *Prevascularization of a fibrin-based tissue construct accelerates the formation of functional anastomosis with host vasculature.* Tissue Engineering - Part A, 2009. **15**(6): p. 1363-1371.

13.   Wu, Y., D.J. Ravnic, and I.T. Ozbolat, *Intraoperative Bioprinting: Repairing Tissues and Organs in a Surgical Setting.* Trends in Biotechnology, 2020.

14.   Pourchet, L.J., et al., *Human Skin 3D Bioprinting Using Scaffold-Free Approach.* Advanced Healthcare Materials, 2017. **6**(4): p. 1601101.

15.   Pourchet, L.J., et al., *Human Skin 3D Bioprinting Using Scaffold-Free Approach.* Advanced Healthcare Materials, 2017. **6**(4).

16.   3d.FAB. *FLOWTIPS®*. 2018; Available from: http://fabric-advanced-biology.univ-lyon1.fr/flowtips/.

17.   Blaeser, A., et al., *Controlling Shear Stress in 3D Bioprinting is a Key Factor to Balance Printing Resolution and Stem Cell Integrity.* Advanced Healthcare Materials, 2016. **5**(3): p. 326-333.

18.   Courtial, E.J., et al., *Silicone rheological behavior modification for 3D printing: Evaluation of yield stress impact on printed object properties.* Additive Manufacturing, 2019. **28**: p. 50-57.

19.   Auxenfans, C., et al., *Use of allogenic epidermal sheets for difficult wound healing: selection and testing of relevant growth factors.* Biomed Mater Eng, 2006. **16**(4 Suppl): p. S73-83.

20.   Gauglitz, G.G., et al., *Hypertrophic scarring and keloids: pathomechanisms and current and emerging treatment strategies.* Mol Med, 2011. **17**(1-2): p. 113-25.

21.   Hinz, B., *The role of myofibroblasts in wound healing.* Curr Res Transl Med, 2016. **64**(4): p. 171-177.

22.   DiPietro, L.A., *Angiogenesis and wound repair: when enough is enough.* J Leukoc Biol, 2016. **100**(5): p. 979-984.

23.   Busuioc, C.J., et al., *Phases of the cutaneous angiogenesis process in experimental third-degree skin burns: histological and immunohistochemical study.* Rom J Morphol Embryol, 2013. **54**(1): p. 163-71.
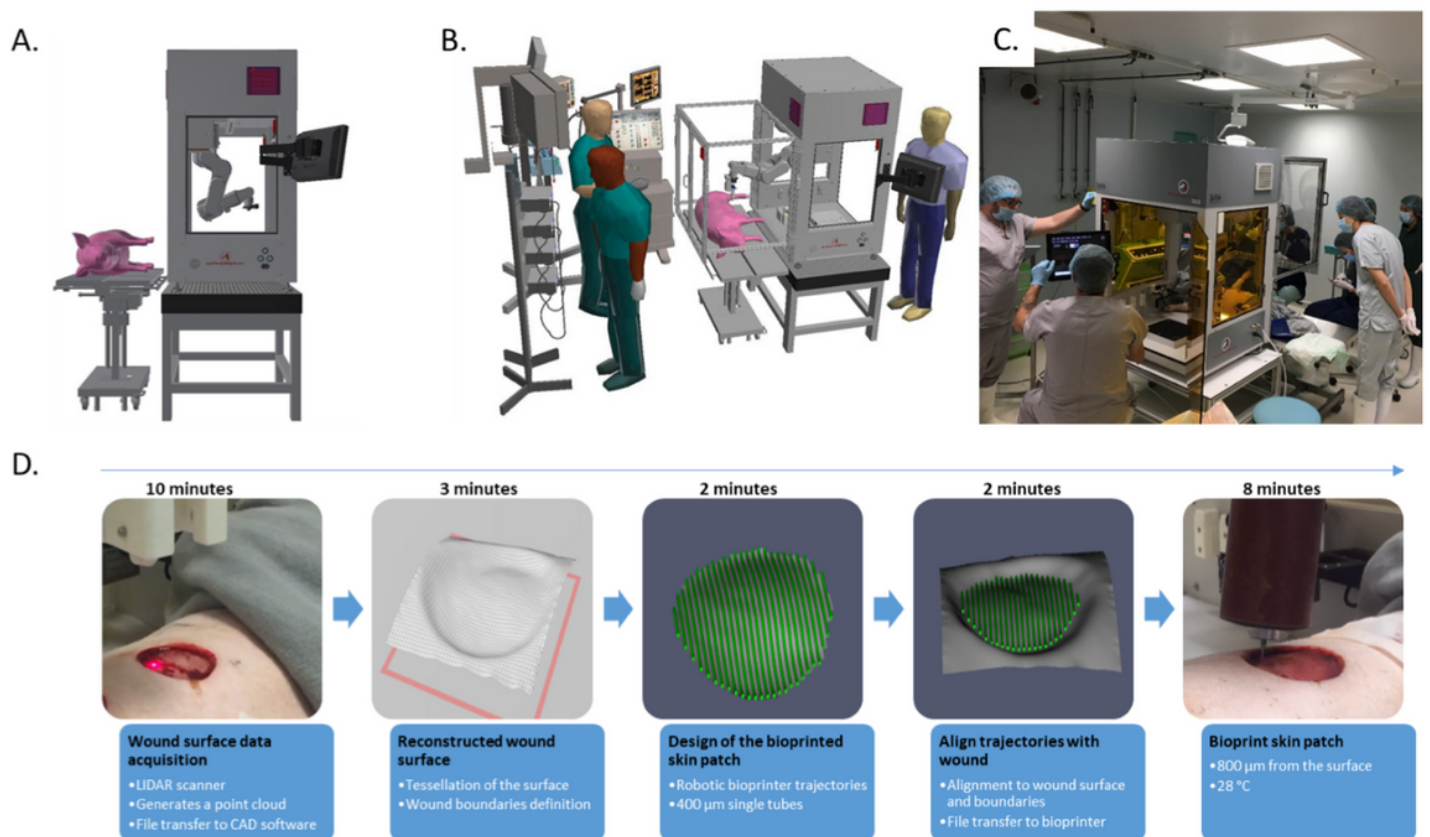
Figures

Figure 1

In vivo bioprinting using a modified BioAssemblyBot. A) The classic BioAssemblyBot configuration. B) The updated BioAssemblyBot with its surgery theatre bioprinting capability. C) The updated BioAssemblyBot actual deployment. D) Workflow of the necessay intraoperative bioprinting steps.
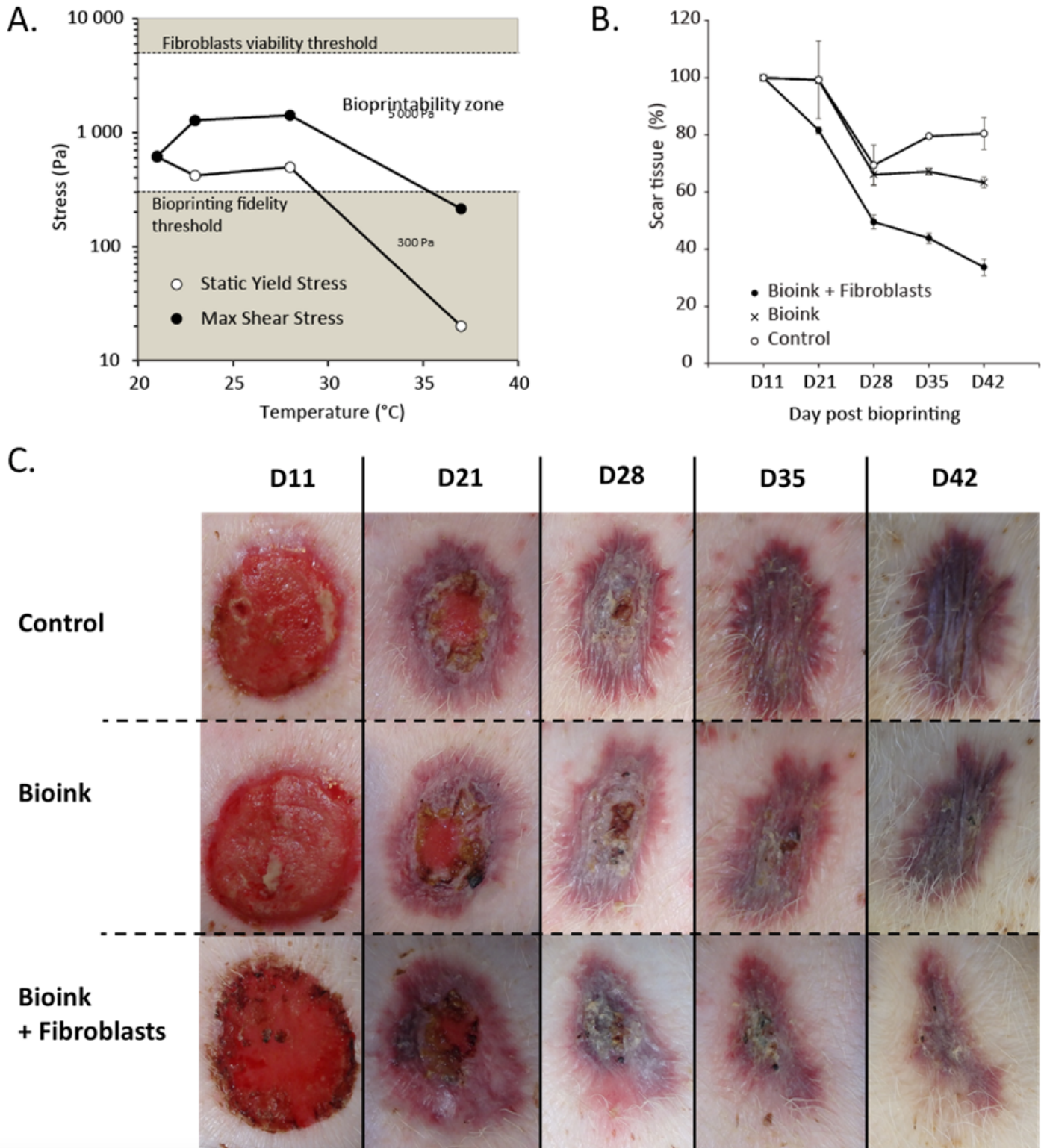
Figure 2

In vivo bioprinting using the modified BioAssemblyBot and wound characterization macroscopic follow up. A) Bioink printability diagram according to shear stress and static yield stress. B) Percentage of scar tissue when compared to D0 (n=2 independent image analysis). D) Characterization follow up for the different experimental conditions (Scale bars are 1 cm).
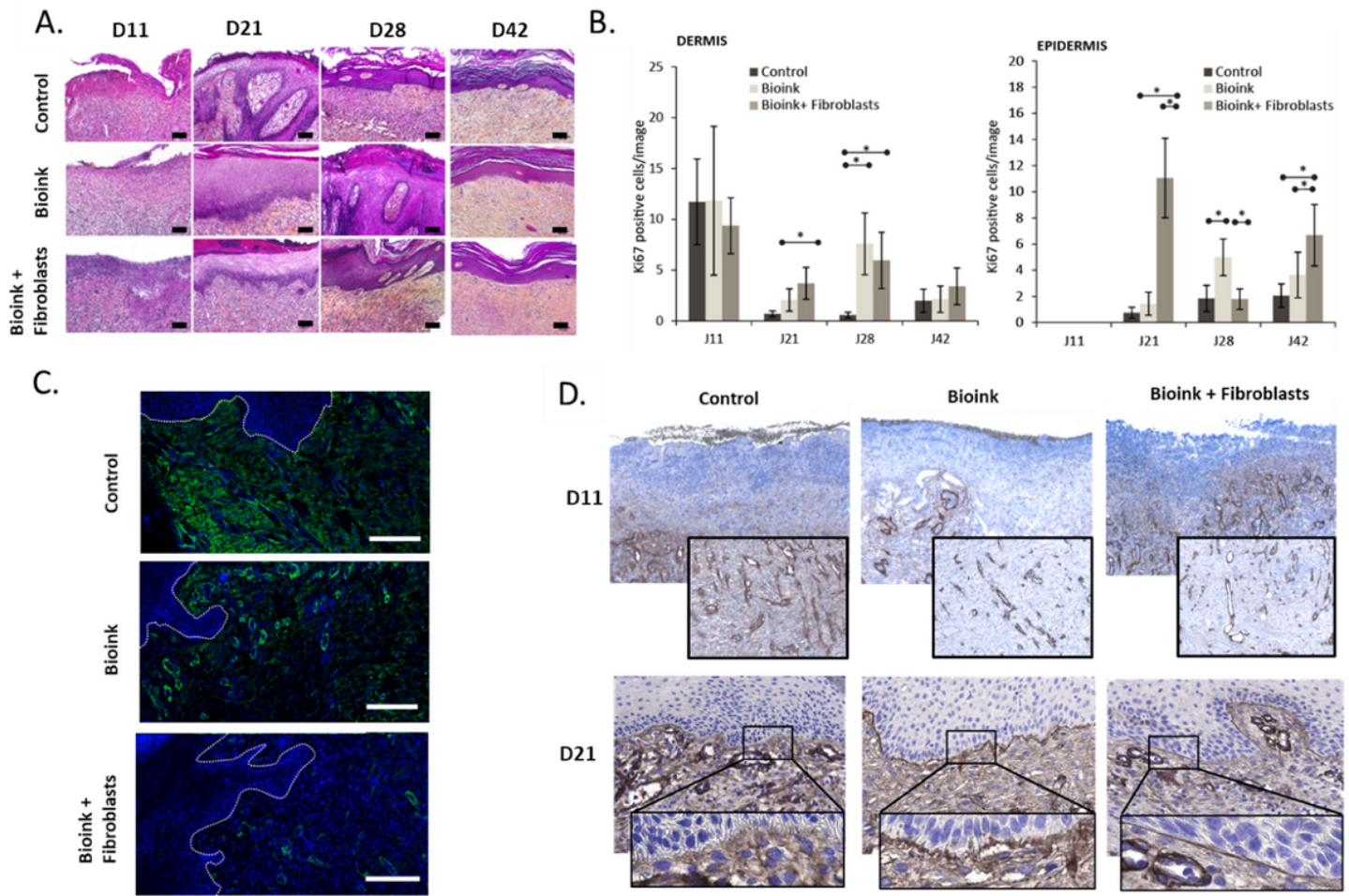
Figure 3

Histological, immunofluorescent and immunostaining characterizations of the wounds during healing. A) Hematoxylin-Phloxin-Saffron staining of the different wounds (scale bar 100 μm). B) Ki67 presence in the different wounds (Pink: Ki67, Blue: cell nuclei, scale bar 100 μm, dash line represents the dermal epidermal junction). C) αSMA presence in the different wounds (centre) at D10 (Green: αSMA, Blue: cell nuclei, scale bar 100 μm, dash line represents the dermal epidermal junction). D) Type IV collagen immunostaining showing DEJ and microvascular structures.